ORCID: 0000-0002-8951-2058

A. V. TITOVA

Bohdan Khmelnytsky National University of Cherkasy, 81 Shevchenko Blvd.,
UA-18031 Cherkasy, Ukraine
titova.anastasiya@vu.cdu.edu.ua

DOI:10.31651/2076-5851-2025-156-173 PACS: 66.30.-h, 07.05.Tp, 64.70.Fx

DECOMPOSITION KINETICS AND PATTERNS FORMATION DURING BINARY ALLOY CO-DEPOSITION AT HIGH DEPOSITION RATES

Monte Carlo simulation of binary alloy co-deposition was revisited for high deposition rates and/or low diffusion rates. Deviations from the "classical" power-law dependence of the steady-state domain size (characteristic length) on deposition rate were obtained. The simulation results were compared with those of the developed semianalytical model.

Keywords: co-deposition, diffusion, Monte Carlo method, decomposition, deposition rate, domain size.

1. Introduction.

The co-deposition of two species from the vapor phase with simultaneous decomposition within the surface and subsurface layers is a technologically important and physically interesting process accompanied by the formation of various patterns, including modulated structures. Such structures open vast opportunities in material design for energy transformation and storage and enable the design of functional devices with large excitonic effects, bandgap modulation, indirect to direct bandgap transitions, piezoelectricity, etc. [1-6]. Thus far, the co-deposition of two components from the vapor phase has been studied mainly by the phase-field method [3-4] or by the artificial Monte Carlo (MC) method simulating the exchanges of whole atomic blocks instead of atoms [7]. In this study, we are shifting our attention to the scale of individual atoms deposition. We will limit ourselves to simplified models of epitaxial deposition on a rigid lattice with coherent interfaces between the phases formed during decomposition, which proceeds simultaneously with co-deposition. Even under such restrictive constraints, the description of phase separation during deposition remains difficult. We will see that the observation of phase separation at the atomic scale requires a high deposition rate and/or a very low diffusion rate. Even if the film geometry remains planar, both of these tendencies lead (as we will see) to significant deviations from "classical" relationships between separation length and "deposition-rate-to-diffusion-rate-ratio". Here, we describe four MC models. Note that in three of these four MC models, the bulk diffusion is treated as completely or almost frozen. Therefore, we do not study here any competition between "vertical" and "lateral" and random concentration modulations (VCM, LCM, and RCM [3,4]): all modulations are "vertical" in our simulations. Only once we include the possibility of exchanges with one atomic plane below (Model 4) and study how this "small" variation of the algorithm may change the dependence of the characteristic length on the deposition rate. Moreover, the characteristic size should depend not only on the deposition rate, but also on the ratio of the deposition rate and surface interdiffusion coefficient. Intuitively, this dependence should be inversely parabolic, $\lambda^2 \sim D/V_{dep}$[1]. We demonstrate that in all models, the deviations from this intuitive dependence increase with increasing V_{dep} / D and also with increasing ratio E_{mix}/k_BT.

In Section 2.1, we discuss the constraints implied in our MC models, taking into account both the "classical" Movchan-Demchishin criteria [8] for single-component thin film structures,

as well as the peculiarities implied by surface-diffusion-controlled phase separation during the co-deposition of two components. In Section 2.2, we discuss the main alternative algorithms for Monte Carlo co-deposition models.

In Section 3.1, we attempt to understand what changes in the phase separation kinetics may be expected in the case of separation mechanism modifications (using the Atzmon-Srolovitz model [7] as an example). In Section 3.2, we trace the evolution of the characteristic sizes with the deposition time and the corresponding film thickness for various MC models. This evolution always tends toward an asymptotic magnitude. In Section 3.3, we determined the dependence of the asymptotic characteristic sizes on the surface-diffusion-to-deposition ratio. In Section 4, we explain the simulation results using a semianalytical model of co-deposition.

2. Methods and Models

2.1. Characteristic parameters of co-deposition.

In the case of single-component deposition from the vapor phase, the thin film structure is determined by the substrate homologous temperature (with correction due to energy dissipation by the arriving atoms), vapor pressure, deposition rate, and/or normalized energy flux [8-11]. In this study, we considered regimes corresponding to active surface diffusion, frozen bulk diffusion, and columnar or cone-shaped grain structures.

The simultaneous deposition of the two species implies additional constraints on the physical parameters. It should be noted that polycrystalline binary alloys, in principle, may contain boundaries of two basic types between grains: 1) abrupt change in crystallographic orientation – large-angle grain boundary; 2) abrupt change in chemical composition, which may be accompanied by a coherent grain boundary (in the case of spinodal decomposition) or a usual large-angle boundary. The interplay between these two possibilities is complex. In this study, we treated phase separation with a coherent inter-phase interface within the same grain. To avoid complications with distinguishing boundaries between grains with different crystallographic orientations and coherent interfaces between different phases within the same crystallographic grain, we modeled (in this study) the formation of an epitaxial monocrystal with simultaneous separation of components within this monocrystal. A similar case of decomposition was obtained by Karczewski et al.[12] during the co-deposition of PbTe/CdTe heterostructures using molecular-beam epitaxy (MBE). In addition, columnar nanopatterns with coherent interfaces (at least at the initial stage) of the Mn-rich phase were obtained during the MBE growth of Ge-Mn thin films [13].

We simulated the co-deposition of a binary alloy of fixed composition with positive mixing energy with the FCC-lattice on the FCC-substrate with orientations (001) and (111). (In our case, we introduced only nearest-neighbor interactions, and for these interactions, the mixing energy per A-B-bond, $E_{mix} = \phi_{AB} - \frac{\phi_{AA}+\phi_{BB}}{2}$ was taken from 0.2 k_BT to 3.0 k_BT.) Due to positive mixing energy, the atoms A and B prefer to form A-clusters and B-clusters just after deposition as long as they are not "buried" and keep mobility during deposition. This time of atoms enhanced "mobility" (with surface interdiffusion coefficient D) within a surface layer of nanometric thickness δ under deposition with velocity V_{dep} is approximately δ/V_{dep}. During this time, the atoms may be separated by a distance of about

$$\lambda_{\text{diff}} = \sqrt{D \cdot \delta/V_{dep}}\ , \tag{1}$$

so that

$$\lambda_{\text{diff}}{}^2 V_{dep} = const, \text{ or}$$

$$ln\lambda_{\text{diff}} = 0.5 \cdot \ln(1/V_{dep}) + const\ , \tag{2}$$

$$n = \frac{dln\lambda_{\text{diff}}}{dln(1/V_{dep})} = 0.5. \tag{3}$$

We emphasize that the length parameter λ_{diff} characterizes the maximal, but not the actual, separation distance. For example, if the deposition is slow, it is possible (at least at some transient stage) that the newly formed clusters of the minority phase will not only suck out the extra solute atoms from the surrounding majority phase, but will also have some time for ripening/coarsening (growth of larger clusters at the extent of smaller clusters via the majority phase considered within mean-field approximation in the ripening models). However, if the deposition rate is high and the time for surface diffusion is small, one might expect large supersaturation in the surface layer, resulting in the nucleation of a large number of supercritical nuclei and insufficient time for their growth and coarsening. Of course, notions of "high" or "low" deposition rates are relative. At least two non-dimensional parameters can be introduced, including the ratio of the deposition rate and surface interdiffusion rate.

First one is

$$v_1 = \frac{\delta \cdot V_{dep}}{D}. \quad (4)$$

The case of v_1=1 corresponds to $\lambda_{\text{diff}} = \delta$ (thickness of surface diffusion zone – about or less than one nanometer). Intuitively, this implies a very high deposition rate and/or a very slow diffusion rate (cold substrate). Higher deposition rates or lower diffusion rates may lead to amorphization, which we did not consider in this paper). Therefore, our regimes correspond to $v_1 \ll 1$.

Second non-dimensional characteristics of the "deposition rate to diffusion rate ratio" may be important in the case of curved interfaces between separating phases (for example, rod-like geometry of minority phase). In this case, it is natural to introduce one more important characteristic length determined by the Gibbs-Thomson effect, $\lambda_{\text{capillary}} = {\gamma\Omega}/{k_B T}$. Here, γ is the interface tension between the resulting phases after decomposition and Ω is the atomic volume. So, we naturally get the non-dimensional parameter

$$x^* = v_2 = \frac{\lambda_{\text{capillary}}}{\lambda_{\text{diff}}} = \frac{\gamma\Omega}{kT}\sqrt{\frac{V_{dep}}{D\cdot\delta}} = \frac{\gamma\Omega}{k_B T\delta}\sqrt{v_1} \quad (5)$$

In the case of a regular solution model with low mutual solubility, the surface tension between the A-rich and B-rich phases may be evaluated as $\gamma \sim \frac{Z_\perp E_{mix}}{a^2}$, for the (001) orientation of FCC $Z_\perp$should be 4. The surface layer may be evaluated as a lattice constant, $\delta \sim a$. Thus, for E_{mix}/k_BT, the non-dimensional parameter

$$x^* = v_2 \sim \frac{4E_{mix}}{k_B T}\sqrt{v_1}.$$

In most studies, the case $x^* \ll 1$ is considered. Indeed, if the separation distance λ_{diff} is of the order of hundred nanometers [2], and Gibbs-Thomson capillary distance is typically less than a nanometer, one gets $x^* \ll 0.01$. In our simulations, this is not the case - it can be of the order of unity, or even larger, because, as we will see below, in our simulations λ_{diff} can be a few atomic distances (one or a few nanometers), so that x^* may indeed be about unity.

We expect that the variation of parameter $x^* = v_2$ within a broad range (by changing E_{mix}/k_BT and the number of Monte Carlo steps (MCS) per deposited layer) will show significant deviations of actual separation distances from the commonly believed equations (1-3) for theoretical diffusion separation distances, especially for relatively fast deposition or for almost frozen surface diffusion.

In the case of rod-like morphology (isolated spots of B-rich phase) the system is characterized by two lengths - (1) domain size (mean radius of rods cross-sections $\langle r\rangle = \sqrt{\langle \text{Area}_B\rangle/\pi}$, where $\langle \text{Area}_B\rangle$ is a mean cross-section area of one B-rich rod), and (2) mean separation distance $L = 2\langle R\rangle$ between the spots centers, where $\langle R\rangle$ is a mean radius of "responsibility zone" around each spot/rod. This is related to the number of rods (spots) N_B :

$N_B \pi \langle R\rangle^2 \approx \text{Area}_{\text{total}}$, so that

$$\langle R\rangle \sim \frac{1}{\sqrt{N_B}} \quad (6)$$

These two characteristic lengths are independent, except in the limiting case of almost full depletion of the surrounding phase. In this limiting case, the mean radius of the rod cross-sections, **under the condition of almost full depletion between clusters, and in case of small solubilities,** should be proportional to the separation distance $2\langle R\rangle$ and the square root of the A-fraction in the deposited flux:

$$\langle r\rangle \sim \langle R\rangle \sqrt{C_B}$$

In other cases, we only have some interrelation between three parameters - $\langle r\rangle$, $\langle R\rangle$, and supersaturation – in the surrounding phase (see below our semianalytical model in Section 4), which should be optimized by some variational extremum principle.

To study other morphologies, more general characteristic lengths, valid for all cases (rods, lamellar, zigzag, and labyrinth), can be chosen:

The first possibility is $\lambda_{\text{diff}} \sim \frac{2\pi}{k^*}$ where k^* is a wave number corresponding to the maximum of the Fourier transform absolute value for function $C_B(x, y)$.

The second possibility is $\lambda_{\text{diff}} \sim \frac{2Area}{L}$, where Area is the total area $\text{Area}_{\text{total}}$ of the surface, or the area of minority phase $\text{Area}_{\text{minority}}$, or rather the average $\text{Area} = \sqrt{\text{Area}_{\text{total}} \cdot \text{Area}_{\text{minority}}}$ and L is the total length of the interphase interfaces within this area. In the first subcase, $\lambda_{\text{diff}} \sim \frac{2\text{Area}_{\text{total}}}{L} \sim \frac{2N\pi R^2}{N \cdot 2\pi r} \sim \frac{R^2}{r}$; in the second subcase, $\lambda_{\text{diff}} \sim \frac{2\text{Area}_{\text{minority}}}{L} \sim \frac{2N\pi r^2}{N \cdot 2\pi r} \sim r$; and in the third subcase, $\lambda_{\text{diff}} \sim \sqrt{\frac{R^2}{r} r} = R$.

The third possibility involves measuring the average number of intersections of vertical (N_x) and horizontal (N_y) straight lines with interphase boundaries within a rectangle of size $L_x \cdot L_y$. The separation length is then calculated as $\lambda_x \sim \frac{L_x}{N_x}$, $\lambda_y \sim \frac{L_y}{N_y}$, $\lambda_{\text{diff}} \sim \frac{1}{1/\lambda_x + 1/\lambda_y} = \frac{\lambda_x \lambda_y}{\lambda_x + \lambda_y}$

2.2. Monte Carlo models of co-deposition

Three main Monte Carlo atomic-scale deposition algorithms were used. In this Section we will concentrate on Monte Carlo (MC) algorithms: The first MC algorithm was based on the picture of an **atom-by-atom** deposition providing a roughened free surface but also the high probability of individual 3D-cluster formation above this surface. The second algorithm was based on **layer-by-layer-via-atom-by-atom** deposition when each next layer started to be filled (one by one) by the deposited atoms only after full filling of the previous layer. The third algorithm was also **layer-by-layer**, but this time at first each new layer was deposited by **simultaneously filling** all empty sites of this layer, and only after this, they were permitted to exchange with each other, providing 2D decomposition within this layer.

Let us formulate shortly four corresponding models.

Model 1. The vapor phase was realized using a lattice gas model with an FCC structure. New atoms were added to the solid phase randomly, one by one, after a fixed number of exchange attempts between neighboring atoms and empty sites. An atom can join and leave the lattice. The inverse number of exchange attempts is a characteristic of the deposition-to-diffusion ratio. The acceptance or non-acceptance of exchange is determined using the Metropolis algorithm. Typical morphologies obtained using Model 1 are depicted in Fig.1a,b,c.

Model 2. In this model, we place new atoms (one by one) only on the remaining empty sites of one plane. The just-arrived atoms can migrate only within this plane by exchanges with neighboring empty sites in the same plane, according to the Glauber algorithm. The new plane is filled only after full filling of previous plane. Typical morphologies obtained using Model 2 are depicted in Fig.1d,e.

Model 3. In this model, atoms exchange not with empty sites but between each other (also according to the Glauber mechanism). Exchanges start after immediate filling by atoms of the entire new atomic layer (typical picture - Fig.1f).

Model 4. In this model, as a development of Model 3, we permit additional directions of jumps from the surface plane to the plane below (and back).

The second and third models appear more artificial (especially at high deposition rates), but they give more reproducible results. In models 1 and 2, atomic migration was simulated by the exchange of empty sites of the 3D-lattice with randomly chosen neighboring atoms, using the Glauber algorithm. In Model 3, the direct exchanges of atoms within one lattice plane were simulated.

Since Model 1 often leads to artifacts, such as the formation of solid clusters above the surface (surrounded by lattice gas), we used Model 1 mainly for qualitative analysis and illustration of possible morphologies. Dependencies of characteristic lengths (mean interlamellar distance in the case of layered morphology, mean size of minority clusters in the case of rod-like morphology), and mean size of the responsibility region around clusters of minority component were measured mainly within other models.

The **main 2 parameters** of our model are the **composition** of the deposition flux and **"frequency" M** - the number of Monte Carlo Steps (MCS) per one deposited layer. (In the first two models, M is the number of atoms per layer multiplied by the number of MCS per deposited atom.) Typically, one MCS must correspond to one (on average) jump attempt for each atom of the system (models 3 and 4). In models 1 and 2, the number of atoms in the layer changes during deposition, and the notion of MCS becomes less evident. We chose the Monte Carlo Step (number of attempts to exchange vacancies with the nearest atoms) as a double number of sites in one atomic layer.

Let us relate (at least by order of magnitude) the MC simulations main parameter M and the real velocity-to-diffusion rate ratio, including the aforementioned non-dimensional parameters. Physically, one Monte Carlo step corresponds to the mean time per atomic jump, τ_{jump}. By order of magnitude, $\tau_{jump} = \frac{(a/\sqrt{2})^2}{4D} = \frac{(a)^2}{8D}$, where D is the surface diffusivity, 4 corresponds to four possible jump directions within the (001) plane of the FCC lattice, and $a/\sqrt{2}$ is the jump length. The correspondence of M MCS to one deposited layer means, in real time, that $\tau_{jump} \cdot M = \frac{\delta}{V_{dep}}$, where in our specific case of the (001) orientation of deposition and strictly layer-by-layer mechanism, $\delta = a/2$. Then, we obtain $\frac{(a)^2}{8D} \cdot M = \frac{a}{2V_{dep}}$, so that

$$v_1 = \frac{aV_{dep}}{2D} = \frac{2}{M},\ v_2 = \frac{\gamma\Omega}{k_B T\delta}\sqrt{\upsilon 1} \approx \frac{4E_{mix}}{k_B T}\sqrt{\frac{2}{M}}, \quad (7)$$

In our simulations of Model 3, we varied the parameter M from 20 to 20000, and $\frac{E_{mix}}{k_B T}$ - from 0.2 3. At that, we have $0.0001 < v_1 < 0.1$, and $0.002 < v_2 < 0.95$. Typical rod-like and lamellar morphologies obtained using Algorithms 1, 2, and 3 are shown in Fig.1.

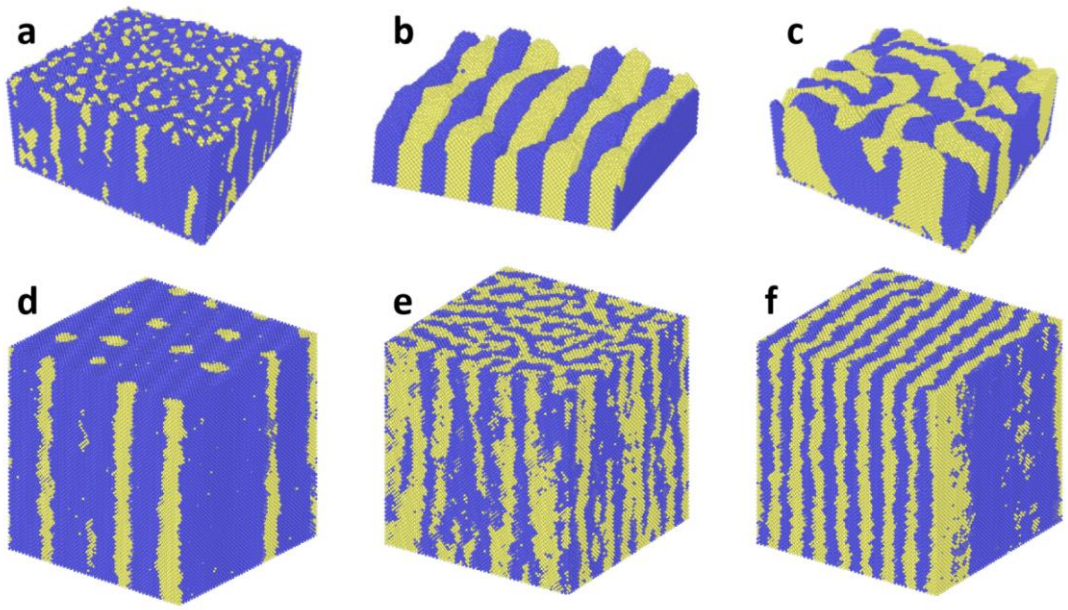

Fig.1. Typical morphologies of co-deposited binary films simulated with Model 1 (atom-by-atom algorithm) at $E_{mix}/k_BT=5$: (a) rod-like (C = 0.16), (b) lamellar (C = 0.50), (c) labyrinth (C = 0.50); Model 2 (layer-by-layer-via-atom-by-atom algorithm) at $E_{mix}/k_BT=0.9$: (d) rod-like (C = 0.10), (e) labyrinth (C = 0.50); and Model 3 (layer-by-layer algorithm) at $E_{mix}/k_BT=0.9$: (f) lamellar (C = 0.50)

Рис. 1. Характерні морфології співосаджених бінарних плівок, сформованих у межах трьох моделей комп'ютерного моделювання для Моделі 1 (алгоритм «атом за атомом») при $E_{mix}/k_BT=5$ спостерігаються: (a) стрижнеподібна морфологія при (C = 0.16), (b) ламелярна морфологія при C = 0.50, (c) лабіринтна морфологія при C = 0.50; Для Моделі 2 (пошарове моделювання через алгоритм «атом за атомом») при $E_{mix}/k_BT=0.9$ отримано: (d) стрижнеподібну морфологію при C = 0.10 та (e) лабіринтну морфологію при C = 0.50; Для Моделі 3 (пошаровий алгоритм) при $E_{mix}/k_BT=0.9$ формується (f) ламелярна морфологія при C = 0.50.

Model 1 was used for qualitative purposes only. Detailed simulations and analytical approximations were performed for planar (or almost planar) models 2, 3, and 4.

In all our simulations, each layer consisted of 5000 sites of the (001) atomic plane with periodic boundary conditions. Quantification of pattern morphology, mixed patterns, and the corresponding memory effects within a simplified kinetic mean-field model can be found in [14].

3. Results

3.1. What happens in the Srolovitz-Atzmon model when we forbid jumps to a neighboring atomic plane.

Atzmon, Srolovitz, et al. [1,7] suggested a theory and simulations of co-deposition. In their simulation, they applied the modified Monte Carlo method for exchanges of atomic "mesoblocks" instead of real atoms. These mesoblocks were deposited layer-by-layer, forming a simple cubic lattice of "quasiatoms". After instant deposition of each layer, quasiatoms obtained a possibility to exchange within this very layer and also with quasiatoms below ("equally weighted exchange attempts are allowed between the site in the topmost layer and all of the 17 first (100), second (110), and third (111) nearest-neighbor sites of the simple cubic lattice surrounding this site." [7]). Simulations of co-deposition for compositions of 0.1 and 0.5 by the authors of [1,7] demonstrated the power laws for the asymptotic (after a few tens or

hundred of deposited layers of quasiatoms) characteristic lengths ⟨r⟩ dependence on the deposition rate. In the case of C=0.5, the morphology was labyrinth-like, and the length was calculated via the number of intersections between straight lines and interphase boundaries.

Approximation by power-like dependencies $\langle r\rangle \sim (1/V_{dep})^n$ in [7] gave n=0.33 for C=0.5 and n=0.37 for C=0.1, instead of "classical" parabolic prediction n=0.5.

We decided to determine how the results of the Atzmon-Srolovitz model change if we completely exclude interlayer exchanges.

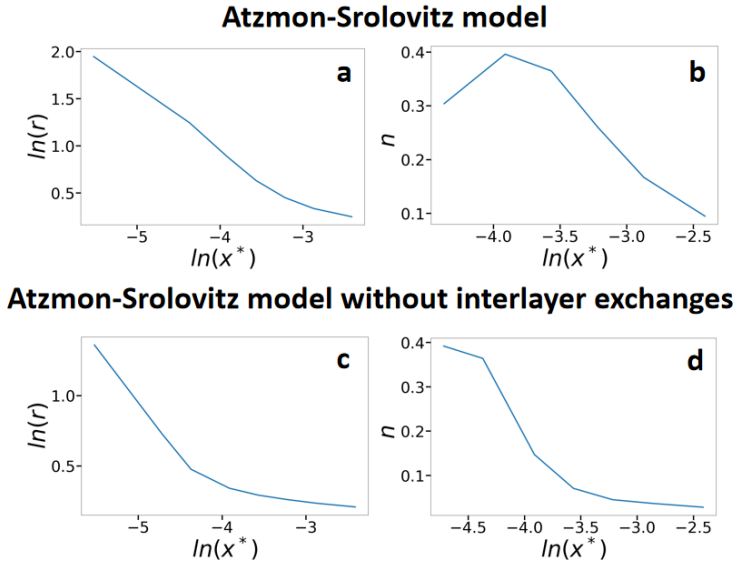

Fig.2. Influence of limitations on diffusion jumps in the Atzmon-Srolovitz model: (a),(c) dependencies of the logarithms of mean domain size ⟨r⟩ on the logarithm of the dimensionless deposition to diffusion ratio x^*; (b), (d) dependencies of exponent $n = dln(\langle r\rangle)/dln(x^*)$ on the logarithm of the dimensionless deposition to diffusion ratio x^*.

Рис. 2. Вплив обмежень на дифузійні стрибки в моделі Атцмона-Сроловіца: (a), (c) наведено залежності логарифма середнього розміру доменів ⟨r⟩ від логарифма безрозмірного співвідношення швидкості осадження до швидкості дифузії x^*; (b), (d) показано залежності показника $n = dln(\langle r\rangle)/dln(x^*)$ від логарифма безрозмірного параметра x^*.

As shown in Fig.2, the exclusion of exchanges with the previous layer changed the scaling laws. The derivative $dln(\langle r\rangle)/dln(x^*)$ is not constant (as explained in Section 4).

3.2. Time/depth dependence of characteristic lengths

Typical dependencies of domain size (characteristic separation length) on the height (deposited atomic layer number) at various values of "frequency" M under the condition of the initial random pattern at the substrate are shown in Fig.3-5. The composition of the initial layer coincided with the composition of the co-deposition flux (C=0.10 or 0.50). Abrupt jumps in some plots correspond to the case when the number of remaining clusters (groups of more than three atoms) is small, and, for example, the joining of one atom to the group of three atoms increases it by 1. As see in Fig.3-5 that after the first few hundred deposited atomic layers, the domain size (characteristic length) reached a steady-state level.

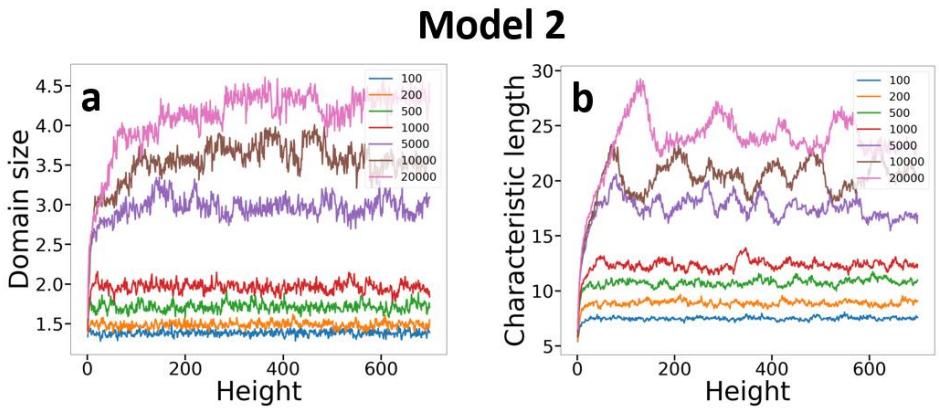

Fig.3. Characteristic length vs height obtained by Model 2 at various values of "frequency" M = 100 MCS/layer; 200 MCS/layer; 500 MCS/layer; 1000 MCS/layer; 5000 MCS/layer; 10000 MCS/layer; 20000 MCS/layer: (a) mean radius ⟨r⟩ of the cross-section of rods vs height (C=0.10); (b) mean characteristic length of the labyrinth structure vs height (C=0.50).

Рис. 3. Залежності характерного розміру від висоти, отримані за Моделлю 2 при різних значеннях «частоти» M: 100, 200, 500, 1000, 5000, 10000 і 20000 MCS/шар. На графіках наведено: (a) залежність середнього радіуса ⟨r⟩ поперечного перерізу стрижнеподібних доменів від висоти при C=0.10; (b) залежність середньої характерної довжини лабіринтної структури від висоти при C=0.50.

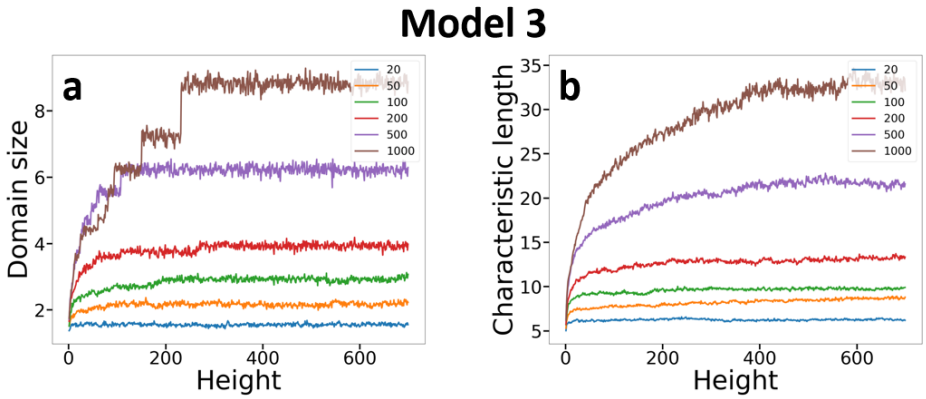

Fig.4. Characteristic length vs height obtained by Model 3 at various values of "frequency" M = 20 MCS/layer; 50 MCS/layer; 100 MCS/layer; 200 MCS/layer; 500 MCS/layer; 1000 MCS/layer: (a) mean radius ⟨r⟩ of the cross-section of rods vs height (C=0.10); (b) mean characteristic length of the labyrinth structure vs height (C=0.50).

Рис. 4. Залежності характерного розміру від висоти, отримані за Моделлю 3 при різних значеннях «частоти» M: 20, 50, 100, 200, 500 і 1000 MCS/шар. На графіках наведено: (a) залежність середнього радіуса ⟨r⟩ поперечного перерізу стрижнеподібних доменів від висоти при C=0.10; (b) залежність середньої характерної довжини лабіринтної структури від висоти при C=0.50.

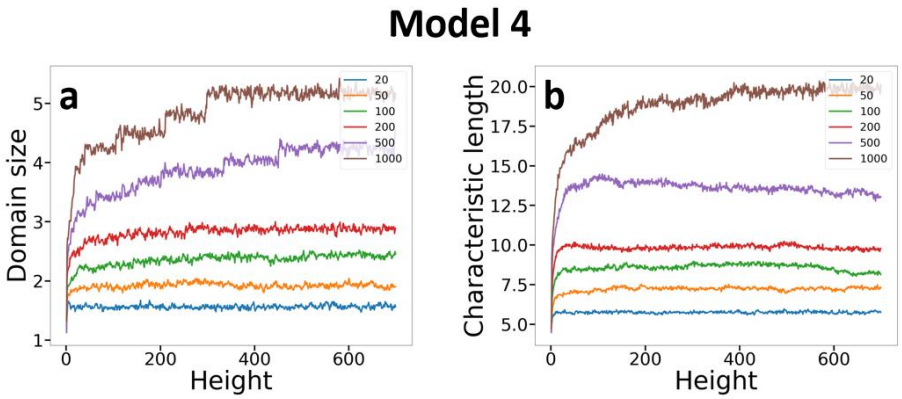

Fig.5. Characteristic length vs height obtained by Model 4 at various values of "frequency" M = 20 MCS/layer; 50 MCS/layer; 100 MCS/layer; 200 MCS/layer; 500 MCS/layer; 1000 MCS/layer: (a) mean radius ⟨r⟩ of the cross-section of rods versus height (C=0.10); (b) mean characteristic length of the labyrinth structure versus height (C=0.50).

Рис. 5. Залежності характерного розміру від висоти, отримані за Моделлю 4 при різних значеннях «частоти» M: 20, 50, 100, 200, 500 і 1000 MCS/шар. На графіках наведено: (а) залежність середнього радіуса ⟨r⟩ поперечного перерізу стрижнеподібних доменів від висоти при C=0.10; (b) залежність середньої характерної довжини лабіринтної структури від висоти при C=0.50

3.3. Steady-state: dependencies of characteristic lengths and areas on deposition/diffusion ratio.

In many cases, the asymptotic morphology under deposition depends only on the deposition conditions (deposition rate, substrate temperature, etc.) and not on the initial conditions. The problem of possible "topological memory" in a range of vapor compositions has been discussed elsewhere. Here, we measured only the characteristic parameters of phase separation ⟨R⟩ and ⟨r⟩ for rod-like geometry and separation length λ_{diff} in the case of the labyrinth (or lamellar or zigzag) geometry of the cross-sections. Typically, the dependencies of these parameters on the deposition-rate-to-surface-interdiffusion-ratio are approximated by power laws such as $\langle R\rangle = \text{const} \cdot x^{*-2k}$, $\langle r\rangle = \text{const} \cdot x^{*-2n}$. We will see below that power law looks like a good approximation only at $x^* \ll 1$. However, we continued to use power exponents in a broad range of parameters:

$$k = -\frac{1}{2}\frac{d\ln\langle R\rangle}{d\ln x^*} \quad (8)$$

$$n = -\frac{1}{2}\frac{d\ln\langle r\rangle}{d\ln x^*} \quad (9)$$

In Fig.6-7 we show the dependencies $\langle r\rangle(x^*)$, $n(\ln x^*)$, $\langle R\rangle(x^*)$, $k(\ln x^*)$ obtained within Models 2, 3, and 4 at C=0.10, E_{mix}/k_BT=0.8. Three runs were performed for each set of parameters. One can see, that the spread of plots remains small, demonstrating the stability of the algorithm.

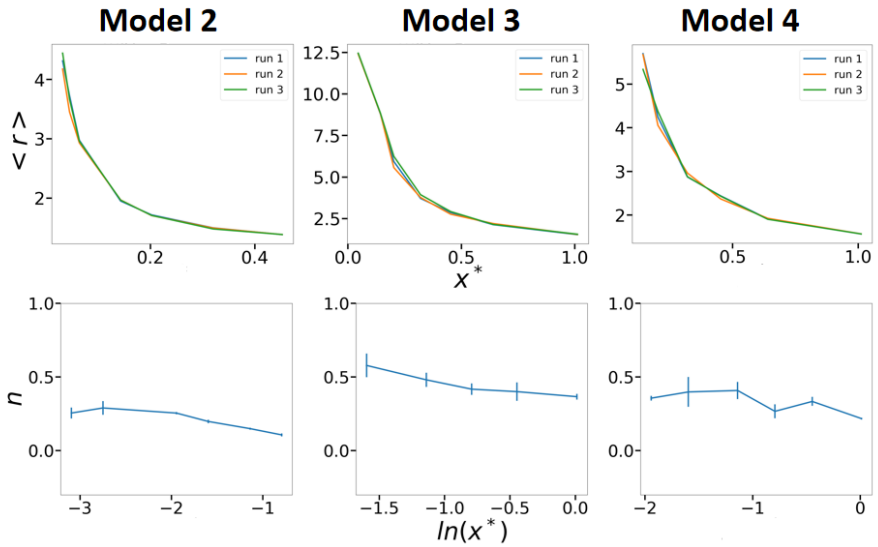

Fig.6. Dependencies $\langle r\rangle(x^*)$ and $n(lnx^*)$ obtained within models 2, 3, and 4 at C=0.10, E_{mix}/k_BT=0.8

Рис. 6. Залежності $\langle r\rangle(x^*)$ та $n(lnx^*)$, отримані в межах моделей 2, 3 і 4 при C=0.10, E_{mix}/k_BT=0.8

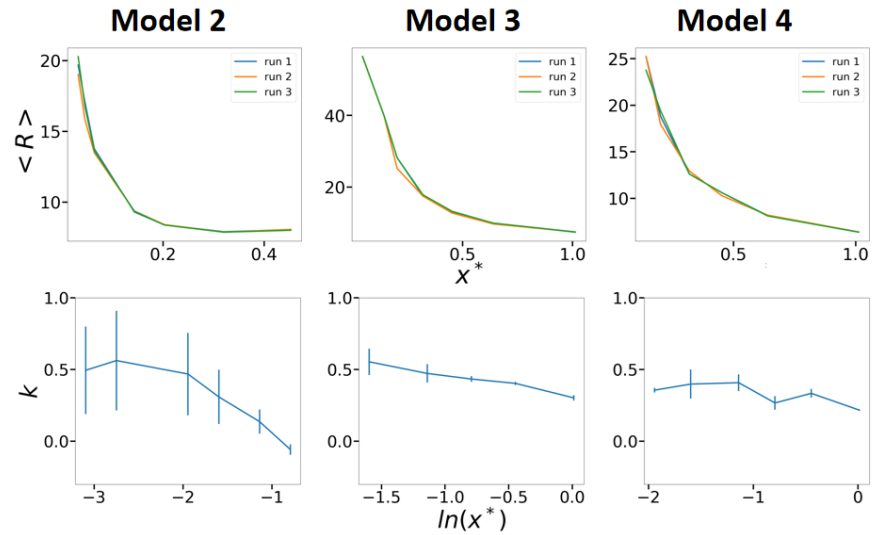

Fig.7. Dependencies $\langle R\rangle(x^*)$ and $k(lnx^*)$ obtained within models 2, 3, and 4 at C=0.10, E_{mix}/k_BT=0.8

Рис. 7. Залежності $\langle R\rangle(x^*)$ та $k(lnx^*)$, отримані в межах моделей 2, 3 і 4 при C=0.10, E_{mix}/k_BT=0.8

In Fig.8, we show the dependencies $\langle\lambda_{diff}\rangle(x^*)$ and $n(lnx^*)$ obtained within Models 2, 3, and 4 at C=0.50, E_{mix}/k_BT=0.8.

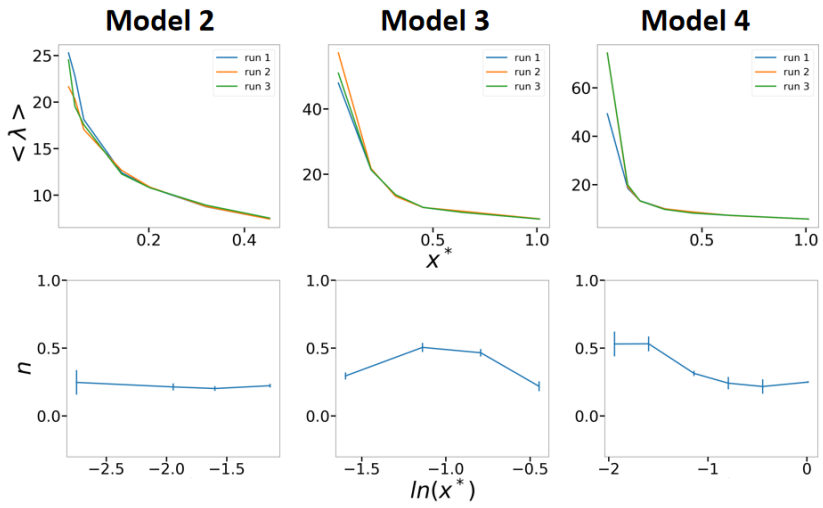

Fig.8. Dependencies $\langle\lambda_{diff}\rangle(x^*)$ *and* $n(lnx^*)$ *obtained within models 2, 3, and 4 at C=0.50,* E_{mix}/k_BT*=0.8*

Рис. 8. Залежності $\langle\lambda_{diff}\rangle(x^*)$ *та* $n(lnx^*)$ *, отримані в межах моделей 2, 3 і 4 при C=0.50,* E_{mix}/k_BT*=0.8*

In Fig.9, we show the dependencies $n(\frac{E_{mix}}{k_BT}, lnx^*)$ obtained within Models 2, 3, and 4 at C=0.10 and 0.50.

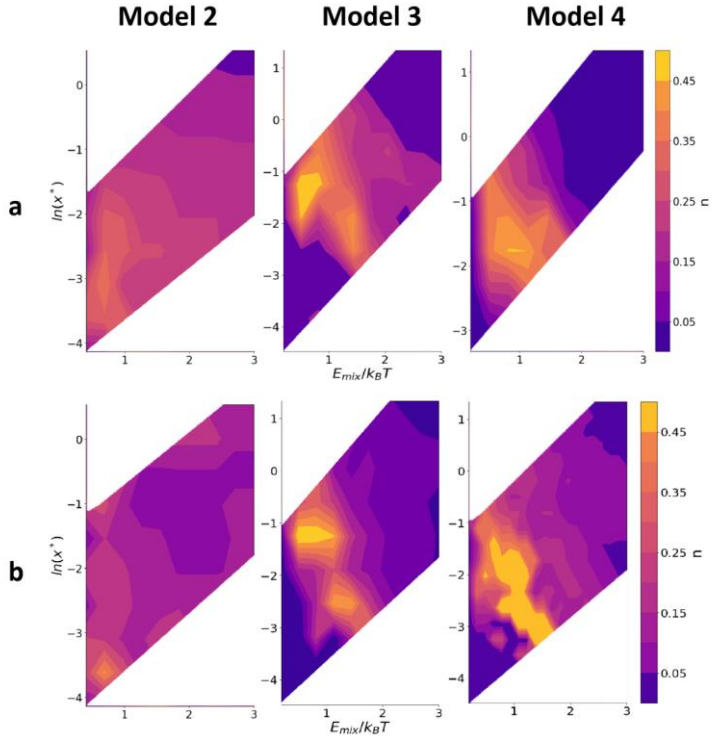

Fig.9. Dependencies $n(\frac{E_{mix}}{k_BT}, lnx^*)$ *obtained within models 2, 3, and 4: (a) at C=0.10; (b) at C=0.50*

Рис. 8. Залежності $n(\frac{E_{mix}}{k_BT}, lnx^*)$ *отримані в межах моделей 2, 3 і 4 при (a) C=0.10 та (b) at C=0.50*

4. Semianalytical description

Semianalytical model of characteristic length dependence on co-deposition rate – neglecting the Gibbs-Thomson effect for equilibrium composition at the curved interfaces.

The results of Monte Carlo simulations show that for the chosen parameters of co-deposition, the dependencies of the separation characteristic length on the deposition rate are far from the well-known prediction $\lambda_{\mathrm{diff}}{}^2 \sim V_{dep}^{-1}$ and, in general, may significantly deviate not only in the magnitude of power exponents but, in general, from the power law itself. Our explanation is based on the assumption that the mentioned regularity should be valid only at a "slow" deposition rate and low temperatures.

Let, as in the third Monte Carlo model, the new atomic layer be deposited momentarily, and then it has time $\Delta t = \frac{\delta}{V_{dep}}$ for decomposition before being buried by the following (next) atomic layer. In our simplified model, the role of the previous layer was to fix the heterogeneous sites of the minority phase to form.

Here, we consider the case of a rod-like morphology with B-rich rods (β-phase) surrounded by an A-rich matrix (α-phase). Let N be the number of heterogeneous sites in the previous layer and the number of rods growing in the rod-like morphology regime. Approximately, $N = \frac{Area_{total}}{\pi R^2}$, where R is the mean radius of responsibility per spot (external radius). (Here, we neglect the effects related to the size distributions and corresponding inequality of $\langle R^2 \rangle$ and $\langle R \rangle^2$.)

Let $r'\left(t < \frac{\delta}{V_{dep}}\right)$ be the time-dependent radius of the growing spot during decomposition.

$R = r'\left(t = \frac{\delta}{V_{dep}}\right)$ is the final radius of the buried spot (inner radius). The region $0<r''<r'(t)$ corresponds to the spot (cross-section of the rod belonging to the minority β-phase).

And the region $r'(t)<r''<R$ correspond to the surrounding majority phase (α-phase).

Of course, in the case of 50/50 alloy, the phase of spot (β-phase) can be called "minority" only formally.

In analogy with Ham's model for the growth of spherical precipitates in 3D, we assume that during the period

$0 < t < \frac{\delta}{V_{dep}}$ the concentration profile in the surrounding phase (majority phase) can be calculated using the quasi-steady-state approximation

$\nabla(D\nabla C) = 0$ Solution of this cylindrically symmetrical problem is:

$$\frac{1}{r''}\frac{d}{dr''}\left(r''D\frac{d}{dr''}C_B\right) = 0 \rightarrow C_B = A\ln\frac{r''}{R} + B = A\ln\zeta + B. \quad (10)$$

We introduce the following non-dimensional parameters:

$\zeta = \frac{r''}{R}$ for points within the surrounding phase, $\eta = \frac{r'}{R}$ for the radius of the spot (rod) during its growth, $\rho = \eta\left(t = \frac{\delta}{V_{dep}}\right) = \frac{r}{R}$ for the final radius after being buried, and this value should tend to be constant in steady-state asymptotics of the co-deposition process.

In formulating boundary conditions for determining the constants A and B, we will use the notation $C_B(R)$ for the boundary condition at the external boundary of the responsibility region and then connect it with other parameters using the conservation of matter. (In the standard Ham's model, it coincides with the initial composition C_{B0}, but in our problem, it could only be if R tends to infinity.)

$$\begin{cases} A\ln\frac{r'}{R} + B = C_{B\alpha'}^{eq}, \\ A\ln\frac{R}{R} + B = C_B(R) \end{cases}, \tag{11}$$

so that

$$A = \frac{C_B(R) - C_{B\alpha}^{eq}}{\ln\frac{R}{r'}} = \frac{C_B(R) - C_{B\alpha}^{eq}}{\ln\frac{1}{\eta}},\ B = C_B(R) = C_B(\zeta = 1) \tag{12}$$

During the time interval $0 < t < \frac{\delta}{V_{dep}}$ the spot grows according to the standard equation for cylindrical phase growth in a supersaturated alloy:

$$\left(C_{B\beta} - C_{B\alpha}^{eq}\right)\frac{dr'}{dt} = D\frac{\partial C}{\partial r''}(r'' = r' + 0) = D\frac{A}{r'} = \frac{D}{r'}\frac{C_B(R) - C_{B\alpha}^{eq}}{\ln\frac{R}{r'}}. \tag{13}$$

$$\text{or } \frac{\ln\frac{R}{r'}}{2D}\frac{\left(C_{B\beta} - C_{B\alpha}^{eq}\right)}{C_B(R) - C_{B\alpha}^{eq}}d(r')^2 = dt \tag{14}$$

Integration over entire time interval gives

$$\frac{D\delta}{R^2 V_{dep}} = \frac{1}{y^2} = \int_{\eta_{min}}^{\rho}\frac{1}{4}\frac{\left(C_{B\beta} - C_{B\alpha}^{eq}\right)}{C_B(R) - C_{B\alpha}^{eq}}\ln\left(\frac{1}{\eta^2}\right)d(\eta)^2 \tag{15}$$

Here $y = \frac{R}{\lambda_{diff}} = R\sqrt{\frac{V_{dep}}{D\delta}}$

If one neglects the nucleation stage then we may take $\eta_{min} = 0$.

Matter conservation gives:

$$C_{B0}\pi R^2 - C_{B\beta}\pi r'^2 = \int_{r'}^{R} dr''2\pi r''C_B(r'') \tag{16}$$

In non-dimensional form it gives

$$C_{B0} - C_{B\beta}\eta^2 = \int_{\eta}^{1} d\zeta \cdot 2\zeta \cdot (A\ln\zeta + B)$$

$$= -\frac{C_B(R) - C_{B\alpha}^{eq}}{\ln\frac{1}{\eta}} \cdot \left(\eta^2\ln\eta + \frac{1-\eta^2}{2}\right) + C_B(R) \cdot (1 - \eta^2) \tag{17}$$

We solve this Eq.(17) in respect to $C_B(R)$:

$$C_B(R) = \frac{C_{B0} - C_{B\beta}\eta^2 + C_{B\alpha}^{eq} \cdot \left(\eta^2 - \frac{1-\eta^2}{\ln(1/\eta^2)}\right)}{1 - \frac{1-\eta^2}{\ln(1/\eta^2)}} \tag{18}$$

Substituting Eq.(18) into Eq.(15), we obtain an equation connecting two unknowns y and ρ (non-dimensional external radius and ratio of inner and external radii):

$$\frac{1}{y^2} = \int_{\eta=0}^{\eta=\rho}\frac{1}{4}\frac{\left(1 - \frac{1-\eta^2}{\ln(1/\eta^2)}\right)\left(C_{B\beta} - C_{B\alpha}^{eq}\right)\ln\left(\frac{1}{\eta^2}\right)}{C_{B0} - C_{B\beta}\eta^2 - C_{B\alpha}^{eq} \cdot (1-\eta^2)}d(\eta)^2 \tag{19}$$

Eq.(19) determines the unknown $y = \frac{R}{\lambda_{diff}}$ if one knows the unknown $\rho = \frac{r}{R}$. So, we need one more equation to find "optimal" ρ.

Following the ideas of John Cahn and many others, let us try the condition of maximum Gibbs free energy release rate: $-\frac{dG}{dt} \longrightarrow \max$. In our model,

$$-\frac{dG}{dt} = -\frac{G^{end} - G^{start}}{\delta/V_{dep}}, \quad G^{end} - G^{start}$$

$$= N\gamma 2\pi r\delta + N \cdot \left(g\left(C_\beta\right) - g(C_0)\right)\frac{\pi(r')^2\delta}{\Omega} + \frac{N}{\Omega}\int_r^R dr''2\pi r''\delta \cdot \left(g\left(C(r'')\right) - g(C_0)\right) \tag{20}$$

In non-dimensional form, the assumption $-\frac{dG}{dt} \to \max$ is:

$$F = -\frac{1}{k_B T}\frac{1}{N\pi R^2}\frac{\Omega}{\delta}\frac{\delta}{V_{dep}}\frac{dG}{dt}$$
$$= -2\frac{x^*}{y}\rho - \left(g(C_\beta) - g(C_0)\right)\rho^2/k_B T - \int_\rho^1 d\zeta"2\zeta \cdot \left(g(C(\zeta)) - g(C_0)\right)/k_B T \to \max \quad (21)$$

$x^* = v_2 = \frac{\lambda_{capillary}}{\lambda_{diff}} = \frac{\gamma\Omega}{kT}\sqrt{\frac{V_{dep}}{D\cdot\delta}} = \frac{\gamma\Omega}{kT\delta}\sqrt{v_1}$, and it, like the energetic part of Gibbs free energy, is proportional to E_{mix}, so that by varying E_{mix} we must simultaneously vary the x^*in Eq.(21)

Typical dependence $F(\rho)$ is shown in Fig.10.

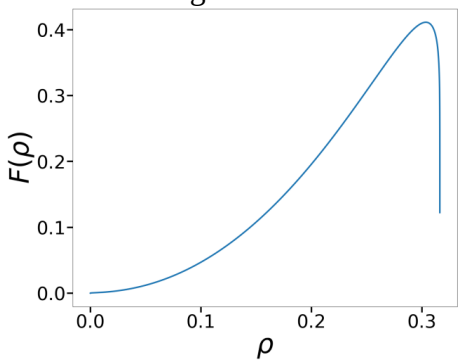

Fig.10. Dependence of the Gibbs free energy release rate on the non-dimensional radius of the spot (cross-section of rod). The maximum of the plot corresponds (according to general though unproven belief) to the optimal characteristic length.

Рис. 10. Залежність швидкості вивільнення вільної енергії Гіббса від безрозмірного радіуса плями (поперечного перерізу стрижня). Вважається, що максимум цієї кривої відповідає оптимальній характерній довжині, хоча це положення має загальноприйнятий, але формально не доведений характер.

We substitute the optimal value of ρ into Eq.(19), and then varying parameter x*, we obtain the dependence between y and x*:

The dependence between lny and $\ln x^*$is shown in Fig.11a.

After finding $\rho_{opt} = \frac{r}{R}$ and $y = \frac{R}{\lambda_{diff}} = R\sqrt{\frac{V_{dep}}{D\delta}}$, we can find the $\frac{r}{\lambda_{diff}} = \frac{r}{R}\frac{R}{\lambda_{diff}} = \rho_{opt}\cdot y$ - see Fig.11b.

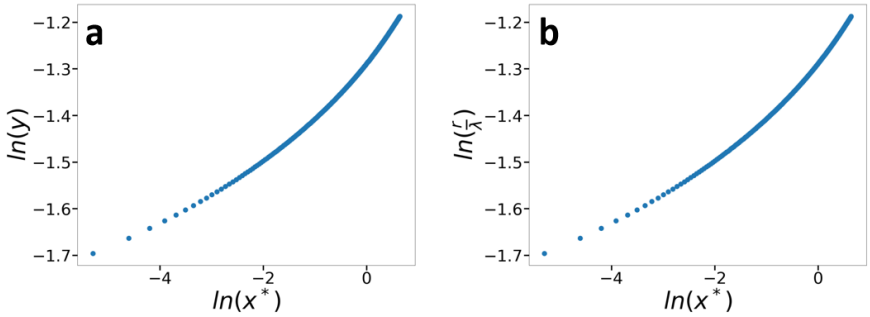

Fig.11. (a) Dependence $ln\left(\frac{R}{\lambda_{diff}}\right) = ln(y)$ *vs* $ln\left(\frac{\lambda_{capillary}}{\lambda_{diff}}\right) = lnx^*$.

(b) Dependence $ln\left(\frac{r}{\lambda_{diff}}\right) = ln(\rho y)$ *vs* $ln\left(\frac{\lambda_{capillary}}{\lambda_{diff}}\right) = lnx^*$

Fig.11. (a) Залежність $ln\left(\frac{R}{\lambda_{diff}}\right) = ln(y)$ *від* $ln\left(\frac{\lambda_{capillary}}{\lambda_{diff}}\right) = lnx^*$.

(b) Залежність $ln\left(\frac{r}{\lambda_{diff}}\right) = ln(\rho y)$ *від* $ln\left(\frac{\lambda_{capillary}}{\lambda_{diff}}\right) = lnx^*$

In the case of linear dependences between logarithms ($\ln\left(\frac{R}{\lambda_{diff}}\right) = pR \cdot \ln\left(\frac{\lambda_{capillary}}{\lambda_{diff}}\right) + const$, $\ln\left(\frac{r}{\lambda_{diff}}\right) = pr \cdot \ln\left(\frac{\lambda_{capillary}}{\lambda_{diff}}\right) + const$), the power dependencies are:

$\left(\frac{R}{\lambda_{diff}}\right) \propto \left(\frac{\lambda_{capillary}}{\lambda_{diff}}\right)^{pR}$, $\left(\frac{r}{\lambda_{diff}}\right) \propto \left(\frac{\lambda_{capillary}}{\lambda_{diff}}\right)^{pr}$, so that

$R = const \cdot (\lambda_{diff})^{1-pR} = const \cdot (x^*)^{pR-1} = const \cdot (x^*)^{-2k_{theor}}$,
$r \propto const \cdot R = const \cdot (x^*)^{pr-1}$

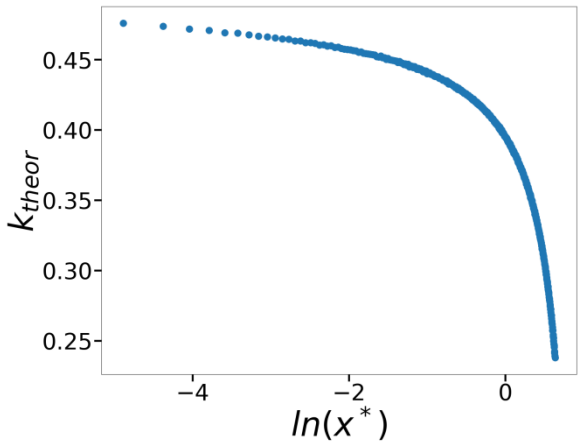

Fig.12. Theoretical dependence of exponent $k_{theor} = -\frac{1}{2}\frac{dln\langle R\rangle}{dlnx^*}$ *vs* lnx^*

Fig.12. Теоретична залежність показника $k_{theor} = -\frac{1}{2}\frac{dln\langle R\rangle}{dlnx^*}$ *від* lnx^*

The theoretical prediction in Fig.12 demonstrates that the exponent decreases from approximately 0.5 to approximately 0.1 with an increasing deposition rate. This is similar to the simulation dependencies in Fig.6-8.

Conclusions

Increasing the deposition-to-diffusion ratio leads to a decrease in the power exponents for the dependence of the characteristic length on the deposition rate.

Increasing the mixing energy-to-temperature ratio also leads to a decrease in the power exponents for the dependence of the characteristic length on the deposition rate.

Acknowledgments

The author would like to thank prof. Andriy Gusak for proposing the research problem and for his insightful guidance, constructive advice, and feedback throughout all stages of this study.

The author thanks the “ENSEMBLE3 - Centre of Excellence for nanophotonics, advanced materials and novel crystal growth-based technologies” project (GA No. MAB/2020/14) carried out within the International Research Agendas programme of the Foundation for Polish Science co-financed by the European Union under the European Regional Development Fund and the European Union’s Horizon 2020 research and innovation programme Teaming for Excellence (GA. No. 857543) for support of this work. We gratefully acknowledge Poland’s high-performance computing infrastructure PLGrid (HPC Centers:

ACK Cyfronet AGH) for providing computer facilities and support within computational grant no. PLG/2023/016228 and for awarding project access to the LUMI supercomputer, owned by the EuroHPC Joint Undertaking, hosted by CSC (Finland) and the LUMI consortium through grant no. PLL/2023/04/016500.

Fruitful discussions with Dr. Oleksandr Malyi and Harshan Reddy Gopidi are appreciated and acknowledged.

Список використаної літератури:

1. Atzmon M. Phase separation during film growth. / M. Atzmon, D. A. Kessler, D. J. Srolovitz // Journal of applied physics. – 1992. – V. 72, No 2, – P. 442-446. Режим доступу: https://doi.org/10.1063/1.351872
2. Adams C. D. Phase separation during co-deposition of Al–Ge thin films / C. D. Adams, M. Atzmon, Y. T. Cheng, D. J. Srolovitz, // Journal of materials research. – 1992. – Vol. 7, No. 3, – P. 653-666. Режим доступу: https://doi.org/10.1557/JMR.1992.0653
3. Powers M. Compositionally-driven formation mechanism of hierarchical morphologies in co-deposited immiscible alloy thin films / M. Powers, J. A. Stewart, R. Dingreville, B. K. Derby, A. Misra, //Nanomaterials. – 2021. – Vol. 11, No. 10, – P. 2635. Режим доступу: https://doi.org/10.3390/nano11102635
4. Lu Y. Microstructure development and morphological transition during deposition of immiscible alloy films / Y. Lu, B. Derby, H. Sriram, K. Kadirvel, C. Wang, X. Liu, Y. Wang // Acta Materialia, 2021, – Vol. 220, – P. 117313. Режим доступу: https://doi.org/10.1016/j.actamat.2021.117313
5. Ko H. Ultrathin compound semiconductor on insulator layers for high-performance nanoscale transistors / H. Ko, K. Takei, R. Kapadia, S. Chuang, H. Fang, P. W. Leu, A. Javey // Nature – 2010. – Vol. 468, No. 7321, – P. 286-289. Режим доступу: https://doi.org/10.1038/nature09541
6. Song J. G. Controllable synthesis of molybdenum tungsten disulfide alloy for vertically composition-controlled multilayer / J. G. Song, G. H. Ryu, S. J. Lee, S. Sim, C. W. Lee, T. Choi, H. Kim // Nature communications – 2015. – Vol. 6, No. 1, – P. 7817. Режим доступу: https://doi.org/10.1038/ncomms8817
7. Adams C. D. Monte Carlo simulation of phase separation during thin-film codeposition / C. D. Adams, D. J. Srolovitz, M. Atzmon // Journal of applied physics – 1993. – Vol. 74, No. 3, – P. 1707-1715. Режим доступу: https://doi.org/10.1063/1.354825
8. Movchan B. A. STRUCTURE AND PROPERTIES OF THICK CONDENSATES OF NICKEL, TITANIUM, TUNGSTEN, ALUMINUM OXIDES, AND ZIRCONIUM DIOXIDE IN VACUUM / B. A. Movchan, A. V. Demchishin // Fiz. Metal. Metalloved – 1969. – Vol. 28, – P. 653-60.
9. Barna P. B. Fundamental structure forming phenomena of polycrystalline films and the structure zone models / P. B. Barna, M. J. T. S. F. Adamik //Thin solid films – 1998. – Vol. 317, No. 1-2, – P. 27-33. Режим доступу: https://doi.org/10.1016/S0040-6090(97)00503-8
10. Thornton J. A. Influence of apparatus geometry and deposition conditions on the structure and topography of thick sputtered coatings/ J. A. Thornton // Journal of Vacuum Science and Technology – 1974. – Vol. 11, No. 4, – P. 666-670. Режим доступу: https://doi.org/10.1116/1.1312732
11. Anders A. A structure zone diagram including plasma-based deposition and ion etching / A. A Anders //Thin Solid Films – 2010. – Vol. 518 No. 15, – P. 4087-4090. Режим доступу: https://doi.org/10.1016/j.tsf.2009.10.145
12. Karczewski G. Nanoscale morphology of multilayer PbTe/CdTe heterostructures and its effect on photoluminescence properties / G. Karczewski, M. Szot, S. Kret, L.

Kowalczyk, S. Chusnutdinow, T. Wojtowicz, L. W. Molenkamp //Nanotechnology – 2015. – Vol. 26, No. 13, – P. 135601. Режим доступу: https://doi.org/10.1088/0957-4484/26/13/135601
13. Mouton I. Composition and morphology of self-organized Mn-rich nanocolumns embedded in Ge: Correlation with the magnetic properties / I. Mouton, R. Lardé, E. Talbot, E. Cadel, C. Genevois, D. Blavette, M. Jamet // Journal of Applied Physics – 2012. – Vol. 112, No. 11, – Режим доступу: https://doi.org/10.1063/1.4768723
14. Titova A. Memory effects during co-deposition of binary alloys / A. Titova, H. Zapolsky, A. Gusak // Scripta Materialia – 2024. – Vol. 241, – P. 115897. Режим доступу: https://doi.org/10.1016/j.scriptamat.2023.115897

References:

1. Atzmon, M., Kessler, D. A., & Srolovitz, D. J. (1992). Phase separation during film growth. *Journal of applied physics*, *72*(2), 442-446. Retrieved from https://doi.org/10.1063/1.351872
2. Adams, C. D., Atzmon, M., Cheng, Y. T., & Srolovitz, D. J. (1992). Phase separation during co-deposition of Al–Ge thin films. *Journal of materials research*, *7*(3), 653-666. Retrieved from https://doi.org/10.1557/JMR.1992.0653
3. Powers, M., Stewart, J. A., Dingreville, R., Derby, B. K., & Misra, A. (2021). Compositionally-driven formation mechanism of hierarchical morphologies in co-deposited immiscible alloy thin films. *Nanomaterials*, *11*(10), 2635. Retrieved from https://doi.org/10.3390/nano11102635
4. Lu, Y., Derby, B., Sriram, H., Kadirvel, K., Wang, C., Liu, X., ... & Wang, Y. (2021). Microstructure development and morphological transition during deposition of immiscible alloy films. *Acta Materialia*, *220*, 117313. Retrieved from https://doi.org/10.1016/j.actamat.2021.117313
5. Ko, H., Takei, K., Kapadia, R., Chuang, S., Fang, H., Leu, P. W., ... & Javey, A. (2010). Ultrathin compound semiconductor on insulator layers for high-performance nanoscale transistors. *Nature*, *468*(7321), 286-289. Retrieved from https://doi.org/10.1038/nature09541
6. Song, J. G., Ryu, G. H., Lee, S. J., Sim, S., Lee, C. W., Choi, T., ... & Kim, H. (2015). Controllable synthesis of molybdenum tungsten disulfide alloy for vertically composition-controlled multilayer. *Nature communications*, *6*(1), 7817. Retrieved from https://doi.org/10.1038/ncomms8817
7. Adams, C. D., Srolovitz, D. J., & Atzmon, M. (1993). Monte Carlo simulation of phase separation during thin-film codeposition. *Journal of applied physics*, *74*(3), 1707-1715. Retrieved from https://doi.org/10.1063/1.354825
8. Movchan, B. A., & Demchishin, A. V. (1969). STRUCTURE AND PROPERTIES OF THICK CONDENSATES OF NICKEL, TITANIUM, TUNGSTEN, ALUMINUM OXIDES, AND ZIRCONIUM DIOXIDE IN VACUUM. *Fiz. Metal. Metalloved. 28: 653-60.*
9. Barna, P. B., & Adamik, M. J. T. S. F. (1998). Fundamental structure forming phenomena of polycrystalline films and the structure zone models. *Thin solid films*, *317*(1-2), 27-33. Retrieved from https://doi.org/10.1016/S0040-6090(97)00503-8
10. Thornton, J. A. (1974). Influence of apparatus geometry and deposition conditions on the structure and topography of thick sputtered coatings. *Journal of Vacuum Science and Technology*, *11*(4), 666-670. Retrieved from https://doi.org/10.1116/1.1312732
11. Anders, A. (2010). A structure zone diagram including plasma-based deposition and ion etching. *Thin Solid Films*, *518*(15), 4087-4090. Retrieved from https://doi.org/10.1016/j.tsf.2009.10.145

12. Karczewski, G., Szot, M., Kret, S., Kowalczyk, L., Chusnutdinow, S., Wojtowicz, T., ... & Molenkamp, L. W. (2015). Nanoscale morphology of multilayer PbTe/CdTe heterostructures and its effect on photoluminescence properties. Nanotechnology, 26(13), 135601. Retrieved from https://doi.org/10.1088/0957-4484/26/13/135601
13. Mouton, I., Lardé, R., Talbot, E., Cadel, E., Genevois, C., Blavette, D., ... & Jamet, M. (2012). Composition and morphology of self-organized Mn-rich nanocolumns embedded in Ge: Correlation with the magnetic properties. Journal of Applied Physics, 112(11) Retrieved from https://doi.org/10.1063/1.476872
14. Titova, A., Zapolsky, H., & Gusak, A. (2024). Memory effects during co-deposition of binary alloys. *Scripta Materialia, 241*, 115897. Retrieved from https://doi.org/10.1016/j.scriptamat.2023.115897

А. В. ТІТОВА
Черкаський національний університет імені Богдана Хмельницького, 18031, б-р Шевченка, 81, м. Черкаси, Україна
titova.anastasiya@vu.cdu.edu.ua

КІНЕТИКА РОЗПАДУ ТА ФОРМУВАННЯ ПАТЕРНІВ ПІД ЧАС СПІВНАПИЛЕННЯ БІНАРНИХ СПЛАВІВ ЗА ВИСОКИХ ШВИДКОСТЕЙ НАПИЛЕННЯ

DOI:10.31651/2076-5851-2025-156-173 PACS: 66.30.-h, 07.05.Tp, 64.70.Fx

Мета роботи: дослідити кінетику розпаду бінарних сплавів за високих швидкостей напилення.

Методика: Метод Монте-Карло було застосовано для моделювання співнапилення бінарних сплавів за високих швидкостей осадження та/або низьких швидкостей дифузії.

Результати. Було отримано відхилення від «класичної» степеневої залежності розміру домену (характеристичної довжини) від швидкості напилення. Результати моделювання було порівняно з результатами розробленої напіваналітичної моделі.

Висновки. Збільшення відношення швидкості напилення до дифузії призводить до зменшення показника степеня залежності характерної довжини від швидкості напилення. Збільшення відношення енергії змішування до температури також призводить до зменшення показника степеня залежності характерної довжини від швидкості напилення.

Ключові слова: співнапилення, дифузія, метод Монте-Карло, розпад, швидкість напилення, розмір домену.

Одержано редакцією 10.11.2025
Прийнято до друку 09.12.2025

Опубліковано 24.12.2025